Lab on a Chip

Accepted Manuscript

ROYAL SOCIETY OF CHEMISTRY

www.rsc.org/loc

3D-Printed Microfluidic Automation

Anthony K. Au*, Nirveek Bhattacharjee, Lisa F. Horowitz, Tim C. Chang, and Albert Folch

Author Affiliation:

Department of Bioengineering, University of Washington, 3720 15th Ave NE, Box 355061, Seattle, WA 98195-5061, USA.

Corresponding Author:

Anthony Au

3720 15th Ave NE

Box 355061

Seattle WA, 98195-5061

(206) 616-9036

antau@uw.edu

Keywords: 3D-printed microfluidics; fluidic automation; microvalves

Abstract: Microfluidic automation – the automated routing, dispensing, mixing, and/or separation of fluids through microchannels – generally remains a slowly-spreading technology because device fabrication requires sophisticated facilities and the technology's use demands expert operators. Integrating microfluidic automation in devices has involved specialized multi-layering and bonding approaches. Stereolithography is an assembly-free, 3D-printing technique that is emerging as an efficient alternative for rapid prototyping of biomedical devices. Here we describe fluidic valves and pumps that can be stereolithographically printed in optically-clear, biocompatible plastic and integrated within microfluidic devices at low cost. User-friendly fluid automation devices can be printed and used by non-engineers as replacement for costly robotic pipettors or tedious manual pipetting. Engineers can manipulate the designs as digital modules into new devices of expanded functionality. Printing these devices only requires the digital file and electronic access to a printer.

Introduction

The vast majority of microfluidic devices are prototyped in poly(dimethylsiloxane) (PDMS) by replica molding ("soft lithography")[1]. Soft-lithographic automation generally involves PDMS layering, alignment, and bonding. PDMS has become popular among researchers because it has many favorable properties: the material is inexpensive, optically clear, and biocompatible; its molding procedure is safe and easy to learn; and its flexibility allows for integrating elastomeric actuators and optical elements into devices. A few companies have been able to build reliable batch fabrication processes after substantial investments (e.g. Fluidigm). However, PDMS-molded microdevices are difficult to disseminate because they are labor-

intensive to produce, rely on specialized fabrication facilities, and typically need bulky controls without featuring "plug-and-play" connectivity[1].

By shortening the time from prototype to product, 3D-printing enables personalized devices, accelerates R&D, and could help reduce the cost of access to healthcare. In stereolithography (SL)[2], a form of 3D-printing, a focused light source produces quasi-arbitrary 3D shapes in a polymer from a photoresin precursor. To create channels, the walls are polymerized by light followed by drainage of the uncured resin[3], without need for assembly (bonding, alignment, etc.). Plastic modular 3D microfluidic circuits have been built with SL[4-6]. The availability of transparent biocompatible resins opens the possibility of fabricating biomedical devices by SL. Microfluidic devices fabricated in biocompatible resin by SL have been demonstrated for high-throughput cell culture and imaging[7], as well as for immunomagnetic[8] and size-based[9] separation of bacteria. As opposed to PDMS and plastic molding processes, SL design is fully digital, amenable to finite-element modeling, intrinsically modular, and can simplify the path to commercialization[10] (see Supplementary Notes).

To date, SL has lacked the valving functionality of soft lithography. Micromolded PDMS valves and pumps confer fluidic automation to PDMS microfluidics, which has greatly impacted fields from physics and chemistry to cell biology and medicine[11]. However, the production of PDMS valves requires significant engineering expertise and access to costly fabrication facilities. Here we report the first valve entirely built in plastic by SL. We demonstrate efficient valving of microchannels. Valves can be effortlessly added into a digital design as modules to form larger operational units such as multi-way switches and pumps. Building these SL devices only requires the digital file and web access.

Results

Although SL technology obviously imposes resolution limits and materials restrictions on our device design, we have been able to 3D-print valves and pumps for microfluidic devices suitable for cell culture applications. Current commercial SL machines only print in a single resin. We chose to print all our devices in WaterShed XC 11122 resin. This nearly colorless resin (Fig. 1a) does not swell in water, has well-characterized wettability[12], and meets minimum biocompatibility standards (see Supplementary Notes and Fig. S1)[13]. The critical part of the valve consists of a membrane with the minimal target thickness (t = 100 μm; Fig. 1b) printable with the laser used by the commercial printing service. The membrane separates two chambers C_1 and C_2. C_1 (the "control chamber") is filled with pressurized air to deflect the membrane. C_2 contains a nozzle that acts as the exit seat of the valve. The membrane must deflect a target distance d = 200 μm (also imposed by printer's constraints) to contact the nozzle and close the valve (Fig. 1c). The necessary membrane radius r to close the gap d under a certain pressure P can be determined as a first approximation from Eqn. 1, which predicts the (large) deflection y at the center of the (thin) membrane given the Young's Modulus E, the Poisson's ratio v, and thickness t:

$$\frac{Pr^4}{Et^4} = \frac{5.33}{1-v^2} \cdot \frac{y}{t} + \frac{2.6}{1-v^2} \cdot \left(\frac{y}{t}\right)^3 \quad (1)^{14}$$

For WaterShed (E = 2,700 MPa, v = 0.30[15]), which has poor elasticity compared to PDMS (E ~ 2 MPa)[16], Eqn. 1 predicts that a membrane of r = 5 mm deflects by y = 204 μm at P = 2.9 psi; COMSOL simulations predict a 2% lower deflection of y = 200 μm at that P (Fig. 2). Thus we designed all our WaterShed valves with r = 5 mm. The valve (filled with blue dye for visualization) is shown in Fig. 1d,e (Movie S1). Valves are actuated by electronically-controlled pressure pulses.

Our COMSOL loading stress simulations indicate that the membrane is maximally stressed at the point of contact with the external nozzle rim (Fig. 2c), suggesting a possible sealing mechanism. Due to variability in the printing process, the pressure required to fully close a valve can vary from 1 to 6 psi depending on the valve (3.30 ± 1.78 psi; mean ± SD; n = 10). The observed range of values, however, agrees fairly well with our COMSOL model: the membrane (shown at rest in Fig. 2a) is predicted to contact the nozzle at ~2.9 psi (Fig. 2b) and fully seal it at ~5.8 psi (Fig. 2c). In any case, operating the valves at 6 psi ensures successful closure of 100% of the valves and does not damage the valves (we have operated the valves by switching between 0 and 3 psi of control pressure for >15,000 cycles without rupture or apparent fatigue; valves occasionally rupture when control pressures >10 psi are applied). The total internal volume of the fluid chamber at rest is 74.8 µL, of which 11.3 µL becomes displaced during valve closure.

To evaluate the reproducibility of the 3D-printing technique, we imaged two devices by micro-computer tomography (microCT; see Fig. 3). Thickness data obtained from each of the microCT slices was mapped onto a color heat map, as represented in Fig. 3b. The histogram of thickness values is shown in Fig. 3c. The average measured values for *t* across the two membranes are 114.6 ± 15.3 µm and 117.4 ± 21.5 µm (mean ± SD). We note that the variations in thickness are equivalent to approximately two voxels in height (the microCT's resolution is 8.7 µm/voxel). In other words, the microCT's resolution was too small to measure appreciable variations in the thickness of the printed membrane. The distance between the nozzle and the membrane was similarly measured from the microCT slices. For the device shown in Fig. 3a, the measured value for *d* was 236.7 ± 36.2 µm (mean ± SD).

We next characterized the dynamic behavior and the fluidic resistance of the valve by measuring the current that passes through a saline-filled valve while it is being operated. We observed that the valve has a cutoff frequency of ~7 Hz; at this frequency, the valve fully opens for only a negligible fraction of the ~71 ms of its "open period" (Fig. 4a). Additionally, our valve's fluidic resistance exhibits a sigmoidal response to control pressure, with the greatest slope in the 0.5-0.65 psi regime and hysteresis between valve opening and closure (Fig. 4b). This multi-state valving behavior could find applications in microfluidic multiplexers[17], flow regulators[18], and fluidic amplifiers[19]. The valves could also simplify the fabrication of microfluidic logic elements, such as adding machines[20], memory latches[21], shift-registers[22], and autonomous oscillators[23, 24]. We did not measure appreciable valve leakage in the closed-valve state, even though the membrane is not built of a self-sealing material (e.g., PDMS). Valve closing pressures were reproducible over many valve closing cycles (Fig. 4c).

Modular design, the joining together of digital modules prior to fabrication, is a powerful design paradigm widely used in many areas of engineering, such as microelectronics, automotives, and aeronautics. SL can similarly benefit from modular design. Since our valve design is fully specified as an electronic file, it can be digitally connected to other functional modules to easily build more complex devices. A fluidic switch (Fig. 5a schematic) can be built by connecting two valves V_1 and V_2 to a common outlet (Fig. 5b). Different dye outputs are produced by opening the appropriate valves (Fig. 5c-e and Movie S2).

We next asked whether we could reliably 3D-print a pump by digitally joining three valves in series (Fig. 6a,b), since peristaltic pumps can be built with three serially-connected valves[25]. The pump was operated with a standard peristaltic sequence (Fig. 6c-e and Movie S3), with each valve opened for a minimum period T (Fig. S2). The maximum average pumping rate

of ~0.68 mL/min was achieved at T = 75 ms, which corresponds to a cutoff frequency of f = 6.7 Hz for a single valve with equal open and closed periods; see Fig. 6f). Note that the T and f measurements for the pump and the isolated valve are very similar, indicating that the performance of the pump is limited mostly by the performance of its fundamental component.

Valves find widespread uses in cell perfusion applications, which often demand complex fluid switching systems that could be built by SL. We printed a fluid switch by digitally joining four valves (Fig. 7a schematic). The fluid inlets were printed as Luer connectors, while the pneumatic inlets and fluid outlet were printed as barbed male connectors to save space (Fig. 7b). The integrated female Luer connectors and barb connectors allow for leak-proof interfacing with male Luer components and tubing, respectively. After connecting the switch to a 3D-printed cell culture chamber with tubing, we demonstrated device operation with food-coloring dyes (Fig. 7c and Movie S4). We then characterized the switching speed of the system with fluorescent dye pulses (Fig. 7c insets and Fig. 7d). We define $t_{on} = t_{90} - t_{10}$ and $t_{off} = t_{10} - t_{90}$, where t_{10} and t_{90} are the times required for reaching 10% and 90% of maximum fluorescence, respectively. In switching between three valves controlling dye and one valve controlling buffer, we measured average values of t_{on} = 2.53 ± 0.14 s and t_{off} = 2.41 ± 0.05 s at the junction; and t_{on} = 4.93 ± 0.15 s and t_{off} = 4.86 ± 0.33 s (mean ± SD) at the chamber. The similar values for dye application and removal ($t_{on} \sim t_{off}$) demonstrate the symmetrical performance of the system. Measurements between the three valves controlling dye varied by at most 5.8%; this high reliability suggests that the fabrication technique might be suitable for large multi-valve arrays.

We next used the four-valve switch to control stimulation of live cells in a culture chamber. We printed a cell culture chamber without a floor, then bonded it to a PDMS slab. This approach enables integration of different cell-biomaterial interfaces. A PDMS floor optimizes

gas exchange (WaterShed is gas-impermeable), microscopy imaging, and cell attachment. With the four-valve switch, we stimulated CHO-K1 cells with 20 s pulses of ATP solutions and followed their Ca^{2+} responses with the Ca^{2+}-sensitive dye, Fluo-4. Results from 1 of 3 similar experiments are shown in Fig. 8a-d, Fig. S3 and Movie S5. Cells labeled with Fluo-4 were seeded into the chambers, and then allowed to attach to the PDMS floor. Images taken every 4 s reveal increases of fluorescence in response to ATP stimulation (Fig. 8a,b). The continued clear responses to multiple ATP stimuli for over 30 minutes demonstrate the viability of the cells in the 3D-printed chamber Fig. 8c,d. The histogram in Fig. 8e reveals the wide variability of single-cell responses that underlie the population-average trace (upper trace in Fig. 8c). In another experiment, we first recorded multiple responses to ATP, followed by multiple pulses of Alexa 594 dye mixed with ATP (Fig. 8f). While the relatively slow Ca^{2+} responses declined by 44% over the course of the experiment, likely due to desensitization over 15 sequential ATP pulses, the concentration profiles for dye application remained stable within 3.8% over the whole field of view. Thus the stability and reproducibility of the concentration profiles in our 3D-printed system appears to be suitable for cell-based assays such as calcium imaging.

Discussion

As PDMS valves revolutionized microfluidics by introducing automation into PDMS microdevices[11], we envision that the digital manipulation of our valves will produce a variety of devices that will amplify the functionality of SL. The overall performance of our microfluidic perfusion system is similar to that of other setups based on syringe pumps or electronic off-chip valves. Where pneumatic actuation is impractical (e.g. point-of-care), membrane-based valves could be actuated via mechanical pins[26] or piezoelectric actuators[27], 3D-printed “pumping lids”

could be used[28], and/or autonomous fluid switching schemes could substitute computer control[29, 30]. We foresee that this first-generation prototype will be further reduced in size as the resolution of SL improves. Printing resolution and materials choices still place critical constraints on the mechanical performance of the valve (see Eqn. 1; *t* and *r* have an exponential relationship with *y*), so that the performance of our valves and pumps is still inferior to that of their PDMS counterparts, but SL is a fast-improving technology. Fast advances in desktop printers[31, 32], photoresins[33], and multi-material SL printing[31, 34] promise rapid, large improvements in resolution and functionality for biomedical applications.

Despite their present fabrication constraints, we believe that the biggest advantage of our valves is that the user benefits from automated manufacturing, so that virtually anyone with web access can fabricate them, independent of his/her field of knowledge. This feature should enable biomedical scientists in remote, disadvantaged locations to profit from the combined inventiveness of engineers around the world and could facilitate the commercialization of new, unforeseen types of biomedical devices.

Methods

COMSOL simulations of membrane deflection and loading stress

The Structural Mechanics Module of the finite element modeling software, COMSOL 4.3a, was used to perform stress analysis and find out the deformation of the membrane when subjected to different pressure loadings. The CAD file of the membrane and the nozzle was imported into COMSOL. The extent of deflection of the deformed membrane was constrained by the bottom of the nozzle – in order to implement this boundary condition, the top of the membrane and the bottom of the nozzle were treated as a “contact pair”, as a result of which the source and the

destination boundaries were coupled when contact was established. The membrane was defined as a linear elastic material with the physical parameters of WaterShed, and different boundary loading pressures were applied to the bottom of the membrane. The difference in the deflection values for t = 100 μm (the target value) and t = 115 μm (the experimental average value) is negligible. The plots in Fig. 2 show a cross-sectional view of the deflection of the membrane at different pressures, as well as the von Mises stresses on the membrane due to the loading.

Valve device fabrication

Devices were built by FineLine Prototyping, Inc. (Raleigh, North Carolina) on a 3D Systems Viper system (Rock Hill, South Carolina) using WaterShed XC 11122 resin (DSM Somos®, Heerlen, Netherlands) in High-Resolution Mode. The valve membranes are defined by a single pass of the laser beam at each z-layer; thus, the membrane thickness is directly defined by the laser beam diameter. For each valve, only a single external control line needs to be connected to the control cavity in order to operate the valve. However, for device fabrication, there must be both an inlet and an outlet to rinse uncured resin out from the control cavity. For multi-valve devices, to simplify the number of Luer connectors required to properly rinse the device (an operation done by the 3D-printing service), all of the rinse channels are simply routed to small holes in the outer face of the devices. These small holes (see arrows in Fig. S4) are then manually sealed off in our lab using adhesive tape or epoxy.

MicroCT imaging

A script written in MATLAB was used to measure the thickness of the membrane from the cross-sectional microCT images, using Otsu's method of image thresholding. The method

creates a binary image from the grayscale microCT cross-sectional slice images, by using a threshold that results in two classes of pixels (background and foreground) with the minimum combined intra-class variance. Edge detection algorithms were then used to determine the edges of the membrane within the device – the distance between the edges indicated the thickness. The total number of data points for the histogram was 1,017,207, of which 0.98% of the measurements were over 175 μm. The distance between the nozzle and the membrane was similarly measured in every microCT slice that had the nozzle (150 slices), by measuring the distance between the detected edge of the membrane and that of the nozzle bottom (taken along ~350 μm on either side of the central nozzle opening).

Valve/pump pneumatic control setup

The valve control channels were connected to three-way solenoid valves (LHDA0511111H from The Lee Company, Westbrook, Connecticut), which were controlled by a National Instruments NI USB-6501 Digital I/O device and LabVIEW software (Austin, Texas). For the single-valve and switching devices, pressurized fluid was applied to the fluid channels of the device, while the solenoids were used to apply either positive pneumatic pressure to the control channels to close the valves or atmospheric pressure to allow the valves to open. For the pumping device, to enhance the pumping speed we close the valves by pressurizing at 5 psi and we open them by returning the control line to -2.5 psi (vacuum); the solenoids were used to alternatingly apply either positive pneumatic pressure or vacuum to the valves in a defined sequence in order to drive fluid through the pump in a directional peristaltic manner.

Single-valve studies

Due to the positioning of the fluid inlet and outlet in the valve design, bubbles may become trapped within the valves during fluid filling. To minimize the occurrence of bubbles, isopropanol may be introduced into the valves first, which can then be replaced with aqueous solution. For all measurements involving single-valve devices we used a fluid driving pressure of 0.5 psi, including flow rate measurements (Fig. 4b) and valve closure measurements. To measure valve closure, the control pressure applied to the opposite side of the valve membranes was increased in increments of 0.5 psi until fluid movement was no longer observed in a thin capillary (0.25 mm I.D. Tygon tubing) connected to the outlet of a device. The valve closing pressures were calculated as the difference between the fluid driving pressure and the control pressure at which the fluid movement was stopped.

Valve dynamic behavior measurements

A single-valve device was filled with 10 mM KCl solution and a constant voltage of 1V was applied across the inlet and outlet of the device, with an oscilloscope connected in series to the outlet end of the device. The valve was opened and closed by alternatingly applying -2.5 psi and +5 psi of pressure to the control channel, while current was measured in the oscilloscope. The current recorded by the oscilloscope was plotted as a function of time for a variety of actuation frequencies to determine the frequency at which the valve no longer fully opens and closes.

Pump rate measurements

The inlet and outlet of the peristaltic pump device were fluidically connected to open reservoirs filled with colored dye. Prior to each pump rate measurement, the three valves of the pump were

opened and the fluid between the two reservoirs was allowed to equilibrate until there was no hydrostatic pressure difference between the two reservoirs. The pump was operated by applying a six-phase actuation sequence to the valves, with each valve opened for a minimum period *T*. The six-phase actuation sequence shown in Fig. S2 was applied to the three valves of the peristaltic pump, with valves V_1 and V_3 opening for time period *T* and valve V_2 opening for 1.5T. The average flow rate through the pump was calculated based on the transfer of fluid to the outlet reservoir, which was placed on top of a laboratory scale. This average flow rate was plotted as a function of the equivalent valve frequency of $f = 1/2T$ (Fig. 6f).

Thermal bonding of SL resin to various substrates

We developed a simple thermal bonding procedure to bond the WaterShed resin to a variety of important biotechnological surfaces, including glass, polystyrene, and PDMS. We chose to bond our chamber to a 1.5 mm-thick PDMS slab to optimize gas exchange (WaterShed is gas-impermeable), microscopy imaging, and cell attachment (we coat it with poly-D-lysine). Unlike prior work using silane surface modification[35], our bonding only requires treating the secondary substrate (PDMS, polystyrene, glass, etc.) with O_2 plasma and heating both surfaces above the glass transition temperature of the resin (WaterShed's T_g ~38-45 °C). In order to bond the SL resin to PDMS, the PDMS surface was treated with O_2 plasma (60 W, 670 mTorr, 1 min, Zepto plasma system, Diener Electronic GmBH, Ebhausen, Germany) before placing the two layers in conformal contact and baking the assembled structure at 70°C for 30 min. Once the structure cooled down to room temperature, the two materials became permanently bonded.

Calcium imaging

CHO-K1 cells were loaded with 5 μM Fluo-4-AM (Invitrogen), loaded into the perfusion chamber, and allowed to attach in the incubator for 1-2 hours with the bottom PDMS surface elevated to permit gas diffusion. Cells were perfused at flow rates from 2.0 to 3.5 mL/min with 3 different ATP concentrations in 20 s pulses, with 160 s rinses of Hank's Balanced Salt Solution (HBSS, Invitrogen) applied between the stimulations to allow the cells to recover. During fluid switching, a 100 ms delay was added between the closing of the valve controlling the previous solution and the opening of the valve controlling the next solution. Images (4x magnification) were taken every 4 s for calcium imaging, and every 0.5 s for perfusion with 100 ng/mL Alexa 594 (Invitrogen). Similar results were seen in three experiments. In Fig. 8 and Fig. S3, individual pixels were identified based on the strength of their correlation between each pixel's trace and an averaged trace of the response of several individual cells, taken over the second and third stimuli[36]. Positive regions were defined as having at least 15 adjoining pixels with a correlation coefficient of at least 0.5. The traces in Fig. 8c show the average intensity in the 7 x 7 pixel box around the centroid of the region for each cell. Note that WaterShed's small autofluorescence does not significantly impede quantitative fluorescence imaging of flow patterns (Fig. 7c insets) and calcium transients (Fig. 8b).

Acknowledgments

This research was funded by NIH R01 grant NS064387. The authors would like to thank Timothy Cox at the Small Animal Tomographic Analysis Facility (SANTA) at Seattle Children's Research Institute for assistance with microCT imaging.

References:

1. A. Folch, *Introduction to BioMEMS*, CRC Press, Boca Raton, FL, 2013.
2. A. Waldbaur, H. Rapp, K. Lange and B. E. Rapp, *Anal. Meth.*, 2011, **3**, 2681-2716.
3. A. Bertsch, P. Bernhard, C. Vogt and P. Renaud, *Rapid Prototyping Journal*, 2000, **6**, 259-266.
4. P. K. Yuen, *Lab Chip*, 2008, **8**, 1374-1378.
5. K. C. Bhargava, B. Thompson and N. Malmstadt, *Proc. Nat. Acad. Sci. (U.S.A.)*, 2014, **111**, 15013-15018.
6. K. G. Lee, K. J. Park, S. Seok, S. Shin, D. H. Kim, J. Y. Park, Y. S. Heo, S. J. Lee and T. J. Lee, *RSC Advances*, 2014, **4**, 32876-32880.
7. W. Busch, B. T. Moore, B. Martsberger, D. L. Mace, R. W. Twigg, J. Jung, I. Pruteanu-Malinici, S. J. Kennedy, G. K. Fricke, R. L. Clark, U. Ohler and P. N. Benfey, *Nat Meth*, 2012, **9**, 1101-1106.
8. W. Lee, D. Kwon, B. Chung, G. Y. Jung, A. Au, A. Folch and S. Jeon, *Anal. Chem.*, 2014, **86**, 6683-6688.
9. W. Lee, D. Kwon, W. Choi, G. Y. Jung and S. Jeon, *Sci. Rep.*, 2015, **5**.
10. A. K. Au, W. Lee and A. Folch, *Lab Chip*, 2014, **14**, 1294-1301.
11. G. M. Whitesides, *Nature*, 2006, **442**, 368-373.
12. E. Wilhelm, K. Deshpande, F. Kotz, D. Schild, N. Keller, S. Heissler, K. Sachsenheimer, K. Lange, C. Neumann and B. E. Rapp, *Lab Chip*, 2015.
13. http://www.realizeinc.com/wp-content/uploads/2010/09/DSM-ISO-10993_Info.pdf.
14. W. Young and R. Budynas, *Roark's Formulas for Stress and Strain*, McGraw-Hill Professional, 2001.
15. N. Chantarapanich, P. Puttawibul, P. Jeamwatthanachai, K. Sitthiseripratip, S. Sucharitpwatskul and A. Laohaprapanon, *Biomedical Engineering International Conference (BMEiCON)*, 2011, 104-107.
16. Z. Wang, A. A. Volinsky and N. D. Gallant, *J. Appl. Polymer Sci.*, 2014, **131**, 41050.
17. D. W. Lee and Y.-H. Cho, *Lab Chip*, 2009, **9**, 1681-1686.
18. E. W. Lam, G. A. Cooksey, B. A. Finlayson and A. Folch, *Appl. Phys. Lett.*, 2006, **89**, 164105.
19. R. Furlan and J. N. Zemel, *Sens Actuators A: Physical*, 1995, **51**, 239-246.
20. E. C. Jensen, W. H. Grover and R. A. Mathies, *J. Micromech. Microeng.*, 2007, **16**, 1378-1385.
21. J. A. Weaver, J. Melin, D. Stark, S. R. Quake and M. A. Horowitz, *Nat Phys*, 2010, **6**, 218-223.
22. M. Rhee and M. A. Burns, *Lab Chip*, 2009, **9**, 3131-3143.

23. B. Mosadegh, C.-H. Kuo, Y.-C. Tung, Y.-s. Torisawa, T. Bersano-Begey, H. Tavana and S. Takayama, *Nat Phys*, 2010, **6**, 433-437.

24. N. S. G. K. Devaraju and M. A. Unger, *Lab Chip*, 2012, **12**, 4809-4815.

25. M. A. Unger, H. P. Chou, T. Thorsen, A. Scherer and S. R. Quake, *Science*, 2000, **288**, 113-116.

26. W. Gu, X. J. Zhu, N. Futai, B. S. Cho and S. Takayama, *Proc. Nat. Acad. Sci. (U.S.A.)*, 2004, **101**, 15861-16866.

27. M. C. Tracey, I. D. Johnston, J. B. Davis and C. K. L. Tan, *J. Micromech. Microeng.*, 2006, **16**, 1444-1452.

28. S. Begolo, D. V. Zhukov, D. A. Selck, L. Li and R. F. Ismagilov, *Lab Chip*, 2014, **14**, 4616-4628.

29. B. Mosadegh, T. Bersano-Begey, J. Y. Park, M. A. Burns and S. Takayama, *Lab Chip*, 2011, **11**, 2813-2818.

30. P. N. Duncan, T. V. Nguyen and E. E. Hui, *Proc. Nat. Acad. Sci. (U.S.A.)*, 2013, **110**, 18104-18109.

31. http://www.ilios3d.com/en/shop/shop-3d-printing/ilios-ray/ilios-ray-printer-detail.

32. http://oldworldlabs.com/.

33. X. Wang, X. Cai, Q. Guo, T. Zhang, B. Kobec and J. Yang, *Chem Commun*, 2013, **49**, 10064-10066.

34. J. W. Choi, E. MacDonald and R. Wicker, *Int. J. Adv. Manuf. Technol.*, 2010, **49**, 543-551.

35. E. Wilhelm, C. Neumann, K. Sachsenheimer, T. Schmitt, K. Lange and B. E. Rapp, *Lab Chip*, 2013, **13**, 2268-2271.

36. X. A. Figueroa, G. A. Cooksey, S. V. Votaw, L. F. Horowitz and A. Folch, *Lab Chip*, 2010, **10**, 1120-1127.

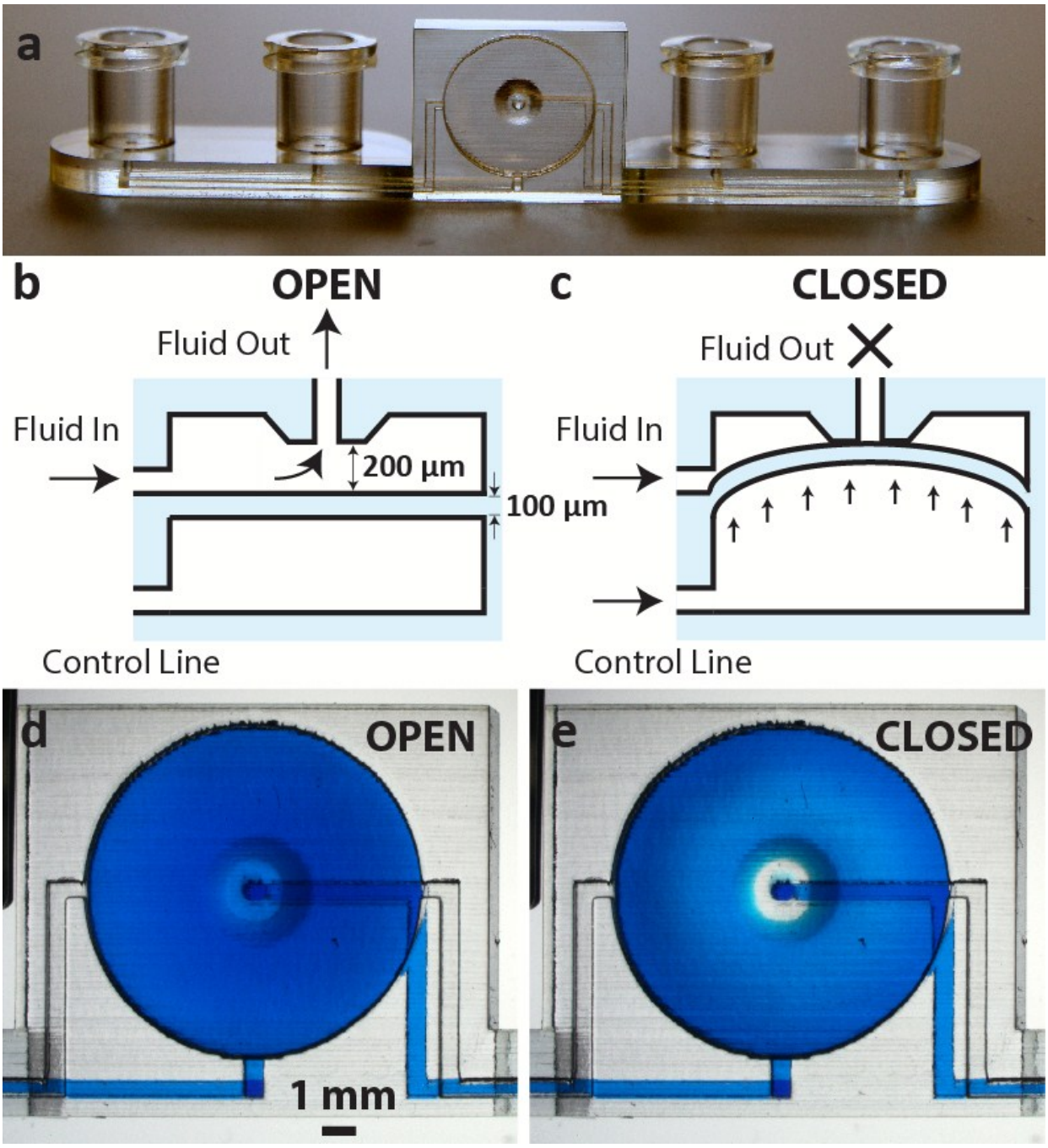

Fig. 1. Basic valve design. (a) Photograph of the single-valve device. (b, c) Schematics of a valve unit in its open (b) and closed (c) states. (d, e) Micrographs of a valve unit in its open (d) and closed (e) states.

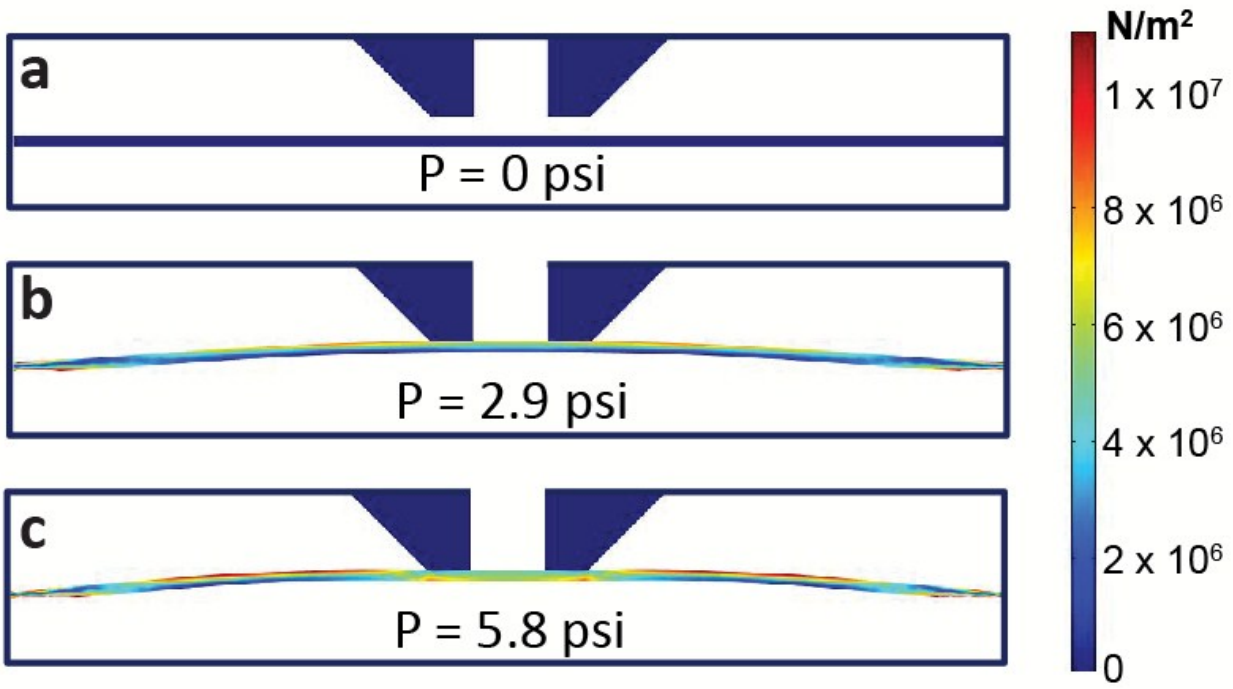

Fig. 2. Membrane deflection simulation. COMSOL simulations of the deflection of the valve membrane at (a) 0 psi, (b) 2.9 psi and (c) 5.8 psi respectively. The color heat map shows the von Mises stress on the membrane at these pressures. The nozzle is positioned 200 μm away from the membrane at rest.

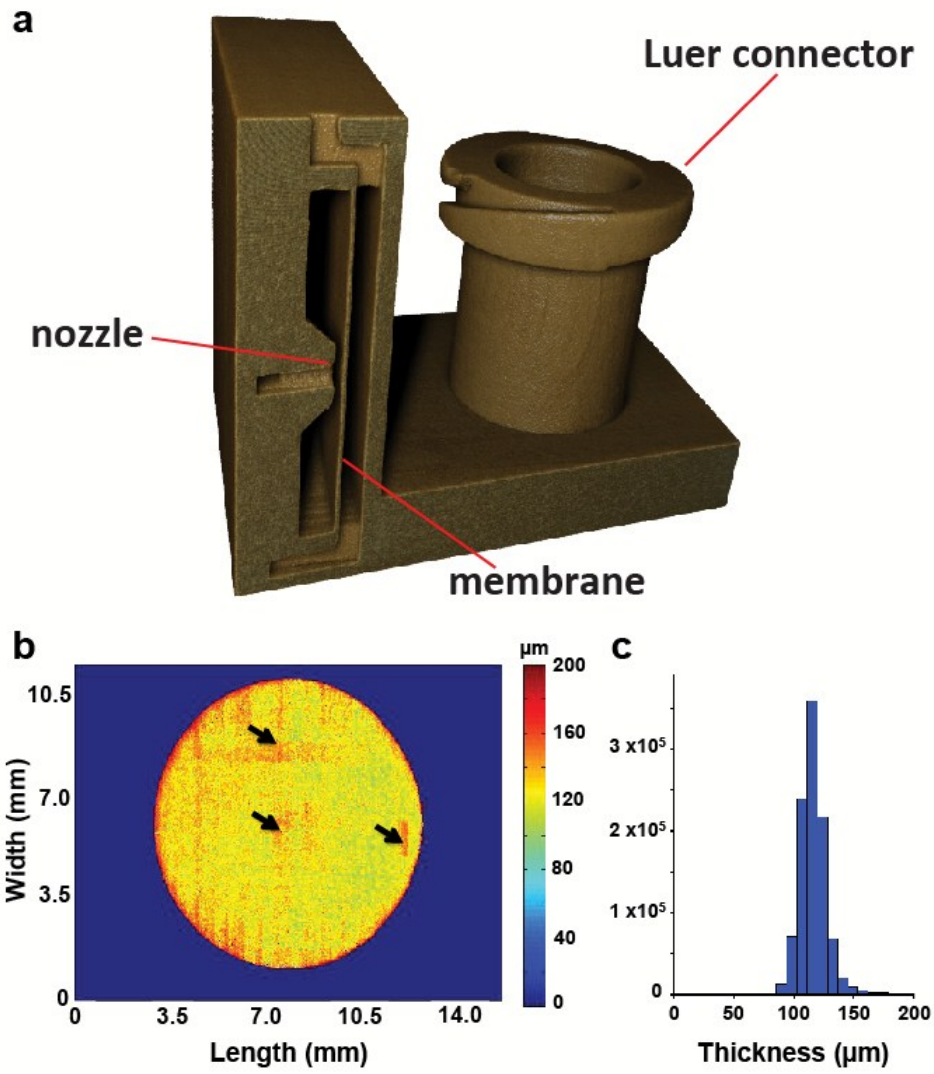

Fig. 3. microCT imaging of membrane. (a) Cross-sectional image of the nozzle and membrane portion of the device obtained by microCT. (b) Color heat map plot of the thickness of the membrane obtained from cross-sectional microCT images, viewed orthogonally. The major irregularities are "phantom features" (arrows) due to out-of-the plane features artifactually introduced by the tomography algorithm. (c) Histogram plot of the membrane thickness (114.62 ± 15.31 μm; mean ± SD). Filtering out the out-of-plane artifacts only changes the average by ~1 μm.

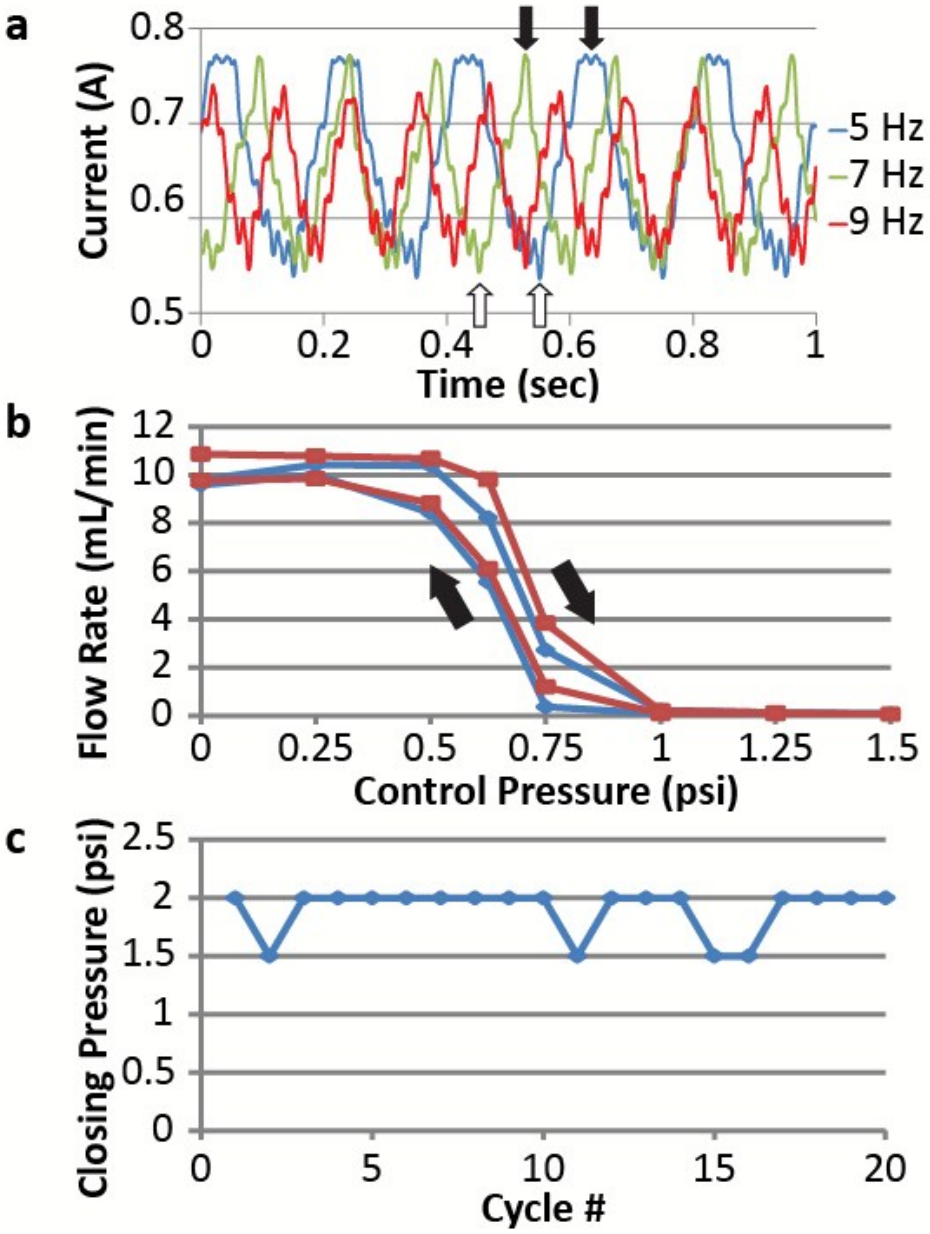

Fig. 4. Single valve characterization. (a) Electrical current crossing the valve at three valve actuation frequencies. The fully open and fully closed states of the valve are indicated by black and white arrows, respectively. (b) Flow rate as a function of the control pressure applied to the valve. (c) The control pressure needed to fully close a valve over 20 opening/closing cycles, showing reproducibility of valve closure.

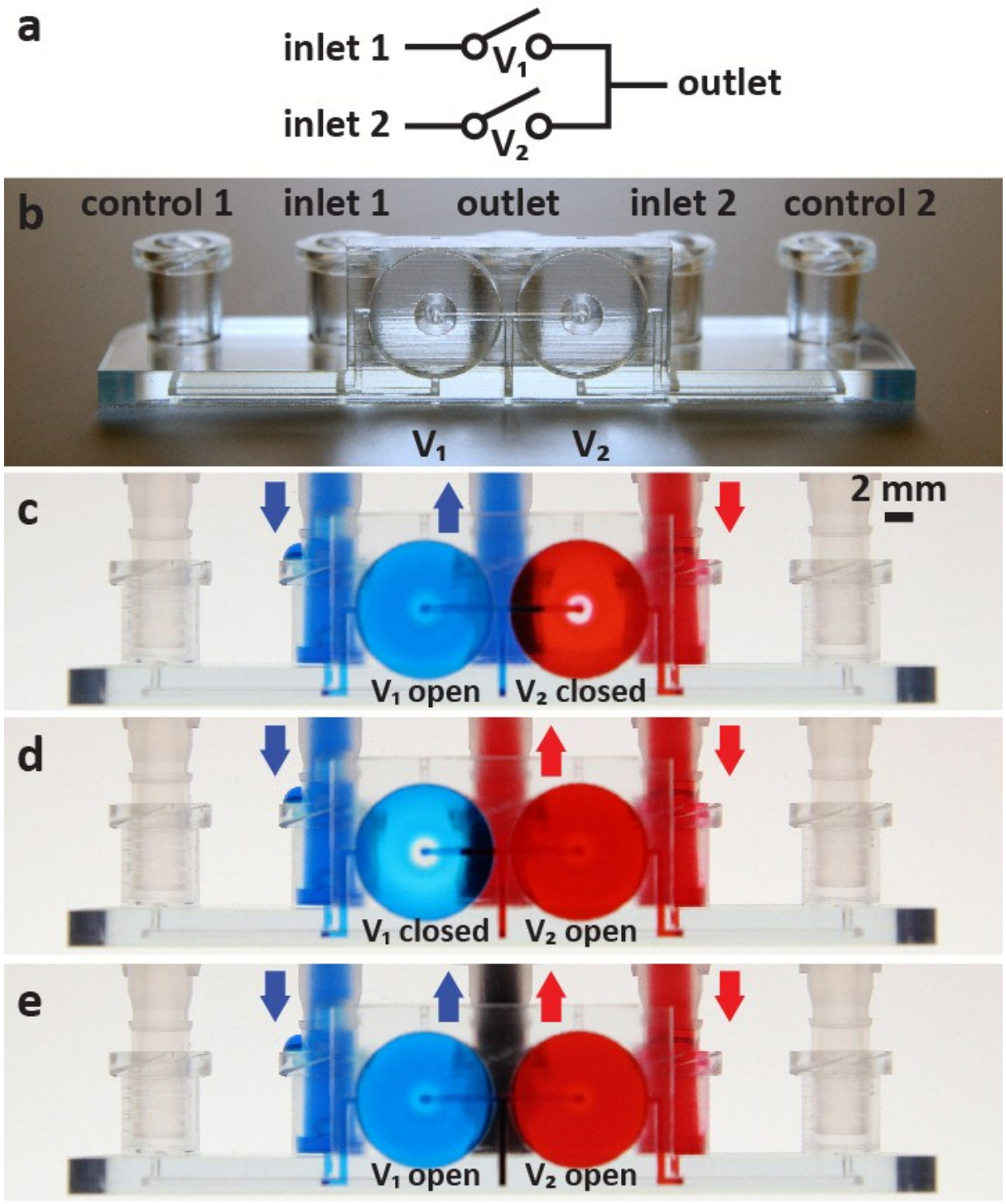

Fig. 5. 3D-printed switch. (a) Circuit diagram and (b) photograph of the two-valve switch. (c-e) Photographs of a dye-filled switch in three different actuation states.

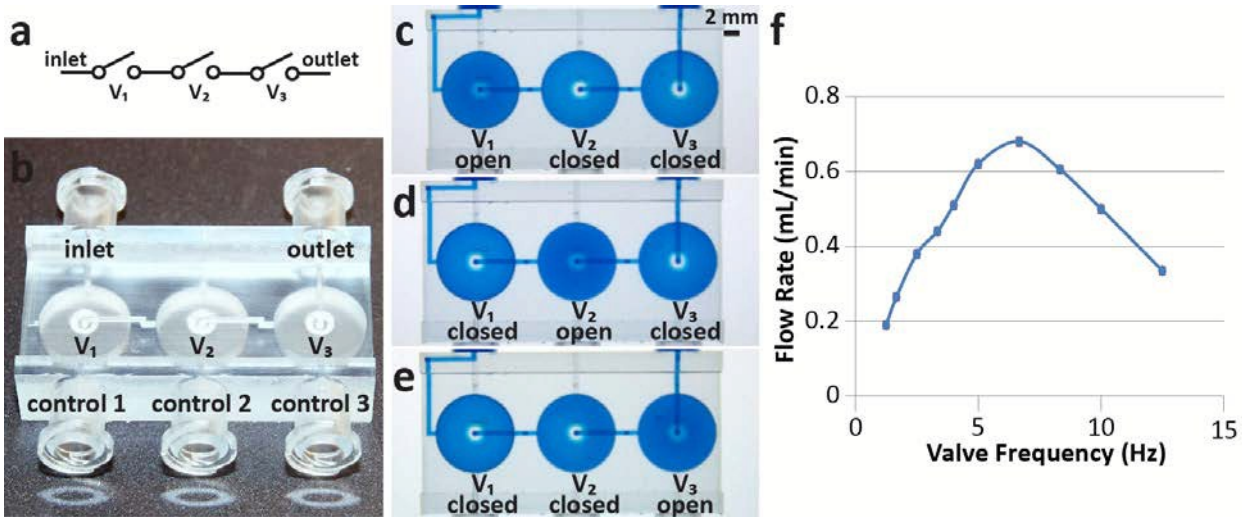

Fig. 6. 3D-printed pump. (a) Circuit diagram and (b) photograph of the peristaltic pump. (c-e) Photographs of a dye-filled pump in three different phases of a peristaltic actuation sequence. (f) Pump rate as a function of pump actuation frequency.

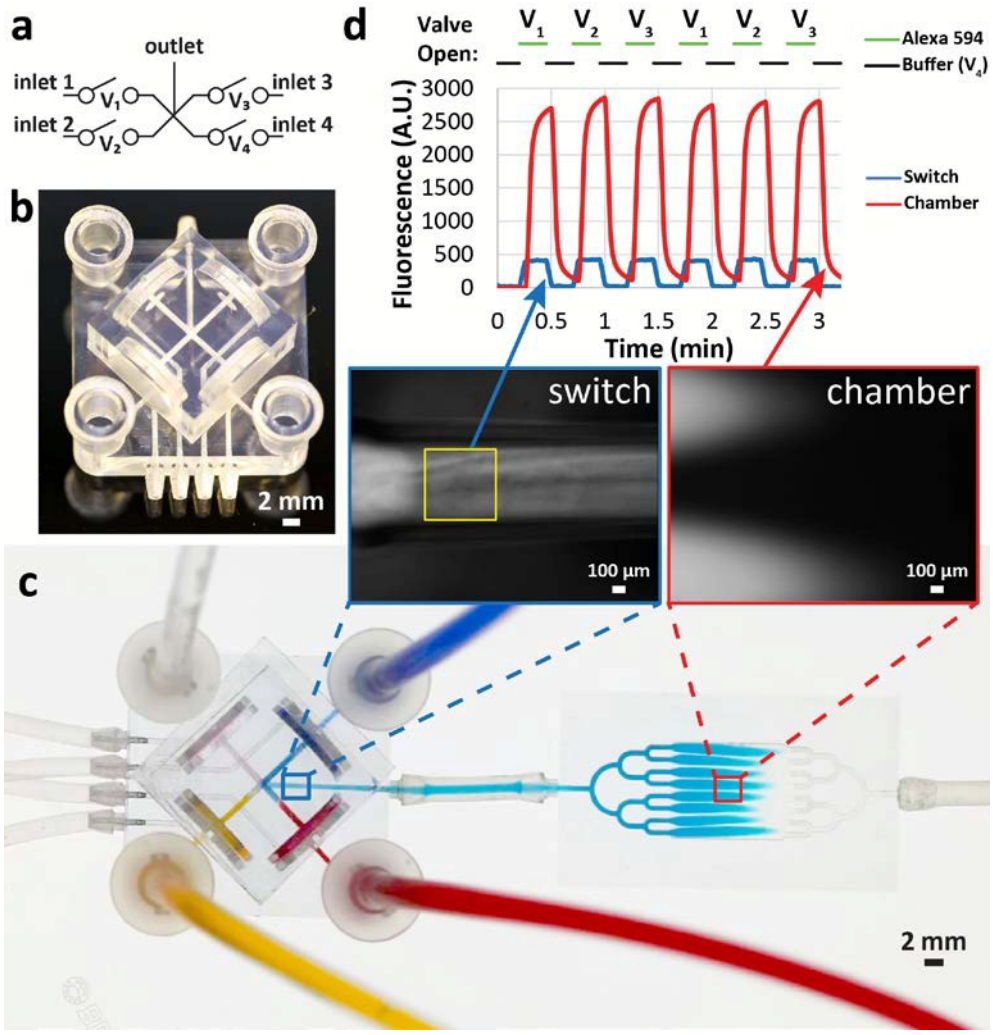

Fig. 7. Valve control of the 3D-printed cell perfusion system. (a) Circuit diagram and (b) photograph of the four-valve switch. (c) Photograph of a dye-filled switch connected to a cell culture chamber (fluorescent micrographs of indicated regions shown as inset). (d) Fluorescence plots showing the concentration profiles in the switch and chamber during fluid-switching events. The red and blue curves correspond to the fluorescence intensity in the cell chamber and the switching device regions, respectively (within the switch, fluorescence was measured within the yellow-boxed region). The top green and black timelines indicate the valve actuation events.

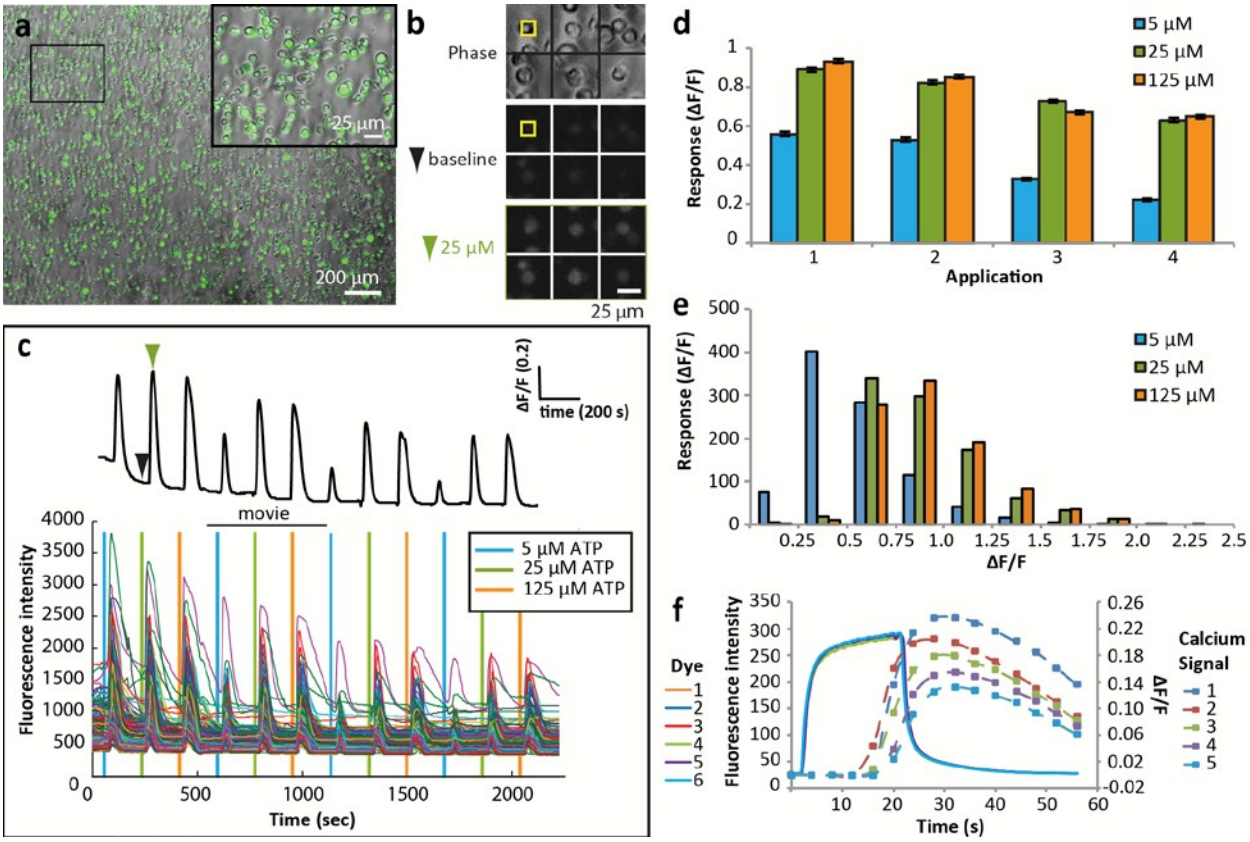

Fig. 8. Calcium imaging with the 3D-printed perfusion system. (a) CHO-K1 cells loaded with calcium indicator dye, Fluo-4, were perfused with a series of 20 s exposures to 3 concentrations (5, 25 and 125 µM) of ATP. Six examples of the 947 cells that responded to ATP are shown in (b) at the time points indicated. A yellow box indicates the central region used to determine average fluorescence. (c) Graphs of calcium responses from the top half of the fluorescent images in (a). The bottom graph depicts the fluorescence traces from 488 individual ATP-responsive cells. The top graph depicts their averaged fluorescence. Arrowheads indicate the times at which the images in (b) were taken. The black bar shows the time frame depicted in Movie S5. (d) The average response (± SEM) to each application for all 947 ATP-responsive cells from the full field of view in (a). (e) The distribution of the responses to the first round of ATP for all 947 ATP-responsive cells. (f) Relative timing and repeatability of stimulus delivery

compared to cellular calcium response. After calcium responses to 5 repeats of 5, 15, and 45 μM ATP were recorded in the green fluorescence channel (only responses to 45 μM shown for clarity), 6 applications of Alexa 594 dye mixed in with the ATP solutions were recorded in the red fluorescence channel using the same perfusion protocol.